Suppression of Temperature Quenching in Perovskite Nanocrystals for Efficient and Thermally Stable Light Emitting Diodes

Mingming Liu,[1,§] Qun Wan,[1,§] Huamiao Wang,[2,§] Francesco Carulli[3], Xiaochuan Sun,[2] Weilin Zheng,[1] Long Kong,[1] Qi Zhang,[1] Congyang Zhang,[1] Qinggang Zhang,[1] Sergio Brovelli[3,] and Liang Li,[1,4,*]*

[1] *School of Environmental Science and Engineering, Shanghai Jiao Tong University, Shanghai 200240, China*

[2] *State Key Laboratory of Mechanical System and Vibration, Shanghai Jiao Tong University, Shanghai, 200240, China*

[3] *Dipartimento di Scienza dei Materiali, Università degli Studi di Milano-Bicocca, 20125 Milano, Italy*

[4] *Shanghai Institute of Pollution Control and Ecological Security, Shanghai 200092, China*

[§] *These authors equally contributed to this work.*

Thermal quenching of light emission is a critical bottleneck hampering the real-world application of lead halide perovskite nanocrystals (PNCs) in both electroluminescent and down-conversion light emitting diodes (LEDs). Here, we report $CsPbBr_3$ PNCs with temperature-independent near unity emission efficiency and constant decay kinetics up to a temperature of T=373 K. This unprecedented regime is obtained by a fluoride post-synthesis treatment that produces F-rich surfaces with a wider energy gap than the inner nanocrystal core, yielding suppressed carrier trapping, improved thermal stability and efficient charge injection. LEDs incorporating these fluoride-treated PNCs show low turn-on voltage, spectrally pure green electroluminescence with external quantum efficiency as high as EQE=19.3% at 350 cd/m^2. Importantly, nearly 80% of the room temperature EQE is preserved at T=343K, in contrast to the dramatic drop commonly observed for standard $CsPbBr_3$ PNC-LEDs. These results provide a promising pathway for high performance practical LEDs based on perovskite nanostructures.

Lead halide perovskite nanocrystals (PNCs), prized for their tunable narrow-band emission, defect tolerance and scalable colloidal synthesis[1], have attracted extensive attention for several photonic and optoelectronic technologies[2-5]. Owing to tremendous advancements in synthetic and post-synthetic chemistry, photoluminescence quantum yield (Φ_{PL}) higher than 90% at room temperature has been demonstrated for PNCs of various compositions[1], leading to substantial progress in the performance of perovskite LEDs (Figure 1)[6-25]. Despite these advancements, one critical bottleneck to the widespread of PNCs-LEDs that is often overlooked is the severe drop of the luminescence efficiency ubiquitously observed at operation temperatures of real-world artificial lighting sources (so called *emission thermal quenching*)[26,27], resulting from the combination of thermally activated carrier trapping and phonon-assisted nonradiative decay. Heat generation is inevitable during LED operation. For example, GaN LEDs used as blue light sources in downconversion LEDs easily reach T=373 K (ref.[28]) and the temperature of the down-converting component is controlled by keeping it far from the blue chip[28] or by using integrated cooling technologies[29]. Unfortunately, such strategies are not applicable to electroluminescent LEDs and adapting the architecture without affecting the device functioning is more complicated and in general less effective in minimizing the thermal damage due to Joule heating in the active layer. For these reasons, strategies for realizing PNCs featuring efficient luminescence fully preserved at elevated temperatures are currently intensively investigated and their achievement would represent a key milestone towards the commercialization of solution-processed PNC-based LEDs.

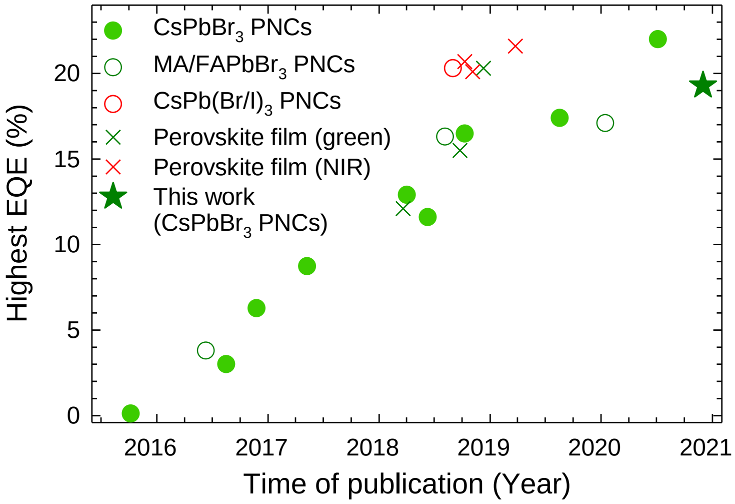

Figure 1. Evolution of lead halide perovskites LEDs performance. Chronological evolution of the EQE of the best green emitting LEDs embedding hybrid fully inorganic[6-14] (full green circles) or organic/inorganic [15-17] (green hollow circles) PNCs compared to thin film devices (green crosses) [19-21] since 2015. Champion LEDs based on PNCs[18] (red circle) or thin films[22-24] (red crosses) emitting in the red/NIR spectral regions are reported for completeness. The champion EQE obtained in this work is shown as a green star.

With this aim, considerable work has been conducted to understand the thermal quenching behavior of PNCs in the T = 10K - 400K range[30]. MAPbBr$_3$ PNCs (MA= methyl ammonium) heated at T=400K have been shown to suffer ~70% loss of their room temperature Φ_{PL}[31] and CsPbBr$_3$ PNCs[32,33] displayed over 80% drop in Φ_{PL} at T=373K. The incorporation of PNCs into polymeric matrixes or silica shells partially mitigates the effect, but it also prevents charge injection, thus rendering the PNCs incompatible with electroluminescent LEDs[30,34,35]. In turn, LEDs based on CsPbBr$_3$ PNCs were shown to lose ~95% of their room temperature electroluminescence (EL) efficiency when operated at T=393 K[36]. As of today, the suppression of emission thermal quenching in PNCs suitable for LEDs is still an open challenge.

In this work, we aim to contribute to address this issue by reporting a fluoride-based post-synthesis treatment that fully suppresses thermal quenching in $CsPbBr_3$ PNCs, resulting in stable Φ_{PL}=90% up to T=370 K and no thermal degradation for successive thermal cycles. Crucially, the resulting surface passivation does not contrast direct charge injection and enables the fabrication of LEDs with EQE as high as 19.3%. Possibly most importantly, thermal stress tests reveal only 23% decrease of the EQE at T=343 K vs. >80% drop commonly observed for conventional PNC-LEDs in the same temperature range[36].

Optical properties and electronic structure of fluoride treated perovskite nanocrystals. $CsPbBr_3$ PNCs were synthesized following the procedure described in the Methods section. For obtaining $CsPbBr_3$:F PNCs, different stoichiometric ratio (0.03, 0.06, 0.12, 0.18, 0.24) of DDAF precursor were mixed with pristine PNCs at room temperatures. The final composition of the treated particles was evaluated by EDS (Supplementary Table 1, Supplementary Figure 1) and the samples were labeled according to the respective F/Br percentage ratio (namely 0.85, 2.4, 3.8, 8.1 and 12%). The F/Br ratio was systematically lower than what expected for the complete occupation of surface bromine sites by fluorine anions, suggesting that F^- occupy surface bromine vacancies and only partially replaced Br^- anions.

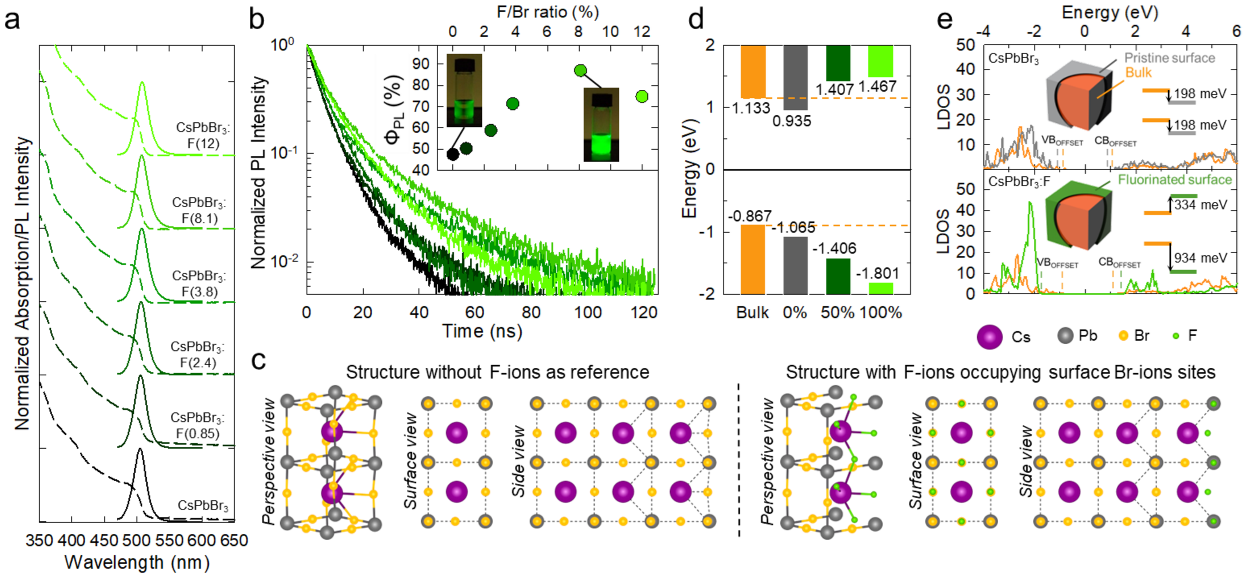

Figure 2. Optical properties and electronic structure of F-treated $CsPbBr_3$ PNCs. (a) Optical absorption (dashed lines) and PL spectra (solid lines, excitation wavelength 400 nm) of pristine (black line) and F-treated (green lines) $CsPbBr_3$ PNCs. The labels indicate the F/Br percentage ratio. (b) PL decay curves and Φ_{PL} (inset) at T=293K. The photographs show toluene solutions of pristine and fluoride treated (F/Br=8.1%) $CsPbBr_3$ (0.4 OD at 365 nm) under 365 nm illumination. The color scheme is the same as for panel 'a'. (c) Calculated atomic structures. (d) Band alignment between bulk layers and surface layers. The bottom and top bars represent the VB and CB respectively. The labels in the *x*-axis indicate the degree of occupation of surface sites by fluorine ions. (e) Local density of states (LDOS) of bulk and surface layers of pristine $CsPbBr_3$ (left panel) and for the same system having F-ions occupying all Br-ions positions (right panel).

In Figure 2a we report the optical absorption and PL spectra of pristine and $CsPbBr_3$·F PNCs, showing essentially identical spectral properties for all systems. The addition of DDAF enhanced the PL efficiency from Φ_{PL}=48±5% of the pristine PNCs to Φ_{PL}=90±7% for $CsPbBr_3$:F(8.1) (Figure 2b). Concomitantly, the PL dynamics lengthened (Figure 2b), suggesting suppression of nonradiative trapping in surface sites. Increasing the F/Br ratio to 12% led to a drop of Φ_{PL} accompanied by the acceleration of the PL dynamics. The use of further excess of fluoride precursor led to degradation of the perovskite structure (Supplementary Figure 2). For this reason, we focused on the comparison between pristine and fluorinated $CsPbBr_3$ PNCs with F/Br ratio up to 8.1%. In order to understand the mechanisms leading to higher Φ_{PL} in fluorine-treated PNCs, as well as to their remarkable PL thermal resistance and EL performance (*vide infra*), we performed density functional theory (DFT)[37] calculations (details in Supporting Information). As shown in Figure 2c, no obvious deformation of the $CsPbBr_3$ surface structure was observed upon the introduction of fluorine ions. The band structure and the local density of states (LDOS) were calculated and displayed in Figure 2d and 2e. For free surface layers of pristine $CsPbBr_3$ NCs, the valence band maximum (VBM) and conduction band minimum (CBM) energies were E_{VBM}=-1.065 eV and E_{CBM} =0.935 eV, respectively. Upon increasing the proportion of F^- ions occupying Br surface sites, E_{VBM} shifted to lower energies and E_{CBM} raised with respect to pristine $CsPbBr_3$. In fluorine treated systems, this leads to the formation of a type-I like junction with large potential barriers for both the VB holes (ΔE_{VBM}= 340-750meV) and the CB electrons (ΔE_{CBM}= 470-530meV) generated in the pure $CsPbBr_3$ PNC core (represented here by the band alignment of pristine PNCs). This explains the observed suppressed nonradiative losses by surface trapping in $CsPbBr_3$:F PNCs. We further calculated the total energy of the systems, E_{TOT}, as a function of the fluorine proportion to probe the stability of the PNCs after fluoride treatment. As shown in Supplementary Table 2, the structure was more stable with increasing fluorine contents, consistent with the highly stable PL under continuous heating (Figure 3).

Thermal resistance experiments. Beside enhancing the emission efficiency, the fluoride treatment has profound effects on the thermal resistance of the luminescence properties of $CsPbBr_3$ PNCs, leading to full suppression of temperature effects up to 373K. To investigate the PL thermal quenching behavior, we monitored the PL of toluene suspensions *in situ* during heating ramps in dark and sealed conditions from T=293K to T=373K (heating rate 10K/min). All measurements were repeated several times to ensure the reproducibility of the PL thermal response. In Figure 3a we report the PL spectra acquired during the heating ramp for pristine $CsPbBr_3$ PNCs and for fluoride treated analogues (F/Br=8.1%). The corresponding integrated PL intensities (normalized to the respective value at T=273 K) as a function of temperature are shown in Figure 3b, together with the data for the whole set of PNCs investigated (the corresponding PL spectra are shown in Supplementary Figure 3).

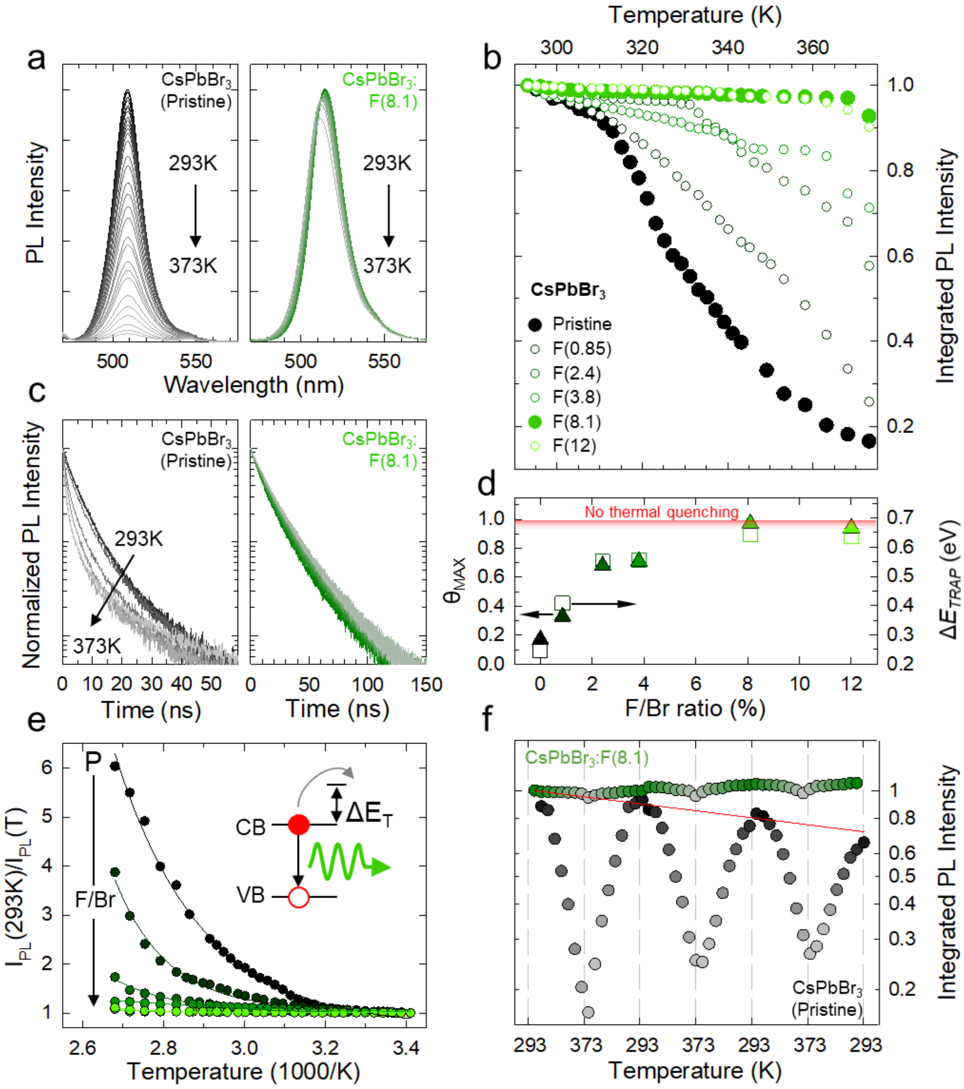

Figure 3. Suppression of emission thermal quenching. (a) PL spectra (excitation wavelength 400 nm), (b) integrated PL intensity and (c) PL decay curves of pristine and F-treated $CsPbBr_3$ PNCs at increasing temperature from 293K to 373K. (d) Temperature resistance (θ_{MAX}) extracted from the data in 'b' and ΔE_{TRAP}-values obtained through the fitting of the data in 'e' as a function of the F/Br ratio in our PNCs. The blurred red bar highlights the condition θ_{MAX}=1, corresponding to zero thermal quenching that is nearly matched by the PNCs with F/Br≥8.1%. (e) Analysis of the PL intensity trend vs. 1000/T fitted to a single trap model. The sold lines are the fitting curves to Eq.1. (f) Integrated PL intensity of pristine and fluoride treated $CsPbBr_3$ during three temperature ramps from 293K to 373K. The red line highlights the thermal degradation of pristine PNCs. The same color code applies to all panels.

In agreement with previous reports[32,38], upon increasing the temperature to 373K, the PL intensity of pristine $CsPbBr_3$ PNCs steeply dropped to ~15% of its room temperature value (corresponding to Φ_{PL}(373K)~7%) and the PL kinetics accelerated by ~90% (from an effective lifetime τ(293K) = 5.4 ns, calculated as the time after which the intensity drops by a factor *e*, to τ(373K) = 0.4 ns, Figure 3c), indicating that carrier trapping was strongly intensified at elevated temperatures. Strikingly, the addition of DDAF boosted the thermal resistance of the PNCs, leading to the perfect temperature independence of the luminescence of $CsPbBr_3$:F(8.1) PNCs for temperatures as high as T=373 K. This is remarkable as it indicates that the fluoride treatment both enhances and preserves the emission efficiency up to elevated temperatures. The evolution with the F/Br ratio resulting from the DDAF treatment of the thermal resistance of the PNCs at 370K, expressed by the term $\theta_{MAX} = \frac{I_{PL}^{370K}}{I_{PL}^{293K}}$ (where I_{PL}^{293K} and I_{PL}^{370K} are the PL intensity at T=293 K and at T=370 K respectively) is highlighted in Figure 3d. With increasing fluorine content, θ_{MAX} grows steeply from ~15% for the pristine PNCs and saturates at ~95% for the $CsPbBr_3$·F(8.1) PNCs, consistent with the passivation of nonradiative traps accessible at 370K, leading to complete suppression of thermal quenching. The invariance of θ_{MAX} for higher F/Br ratios further suggests that excess DDAF amounts are not detrimental for their thermal resistance. Notably, the DDAF treatment was applied also to $CsPbBr_{x\text{-}3}I_3$ and to $CsPbI_3$ PNCs (Supplementary Figures 4,5), resulting, in both cases, in substantial enhancement of the thermal resistance, indicating the generality of the proposed strategy. To further analyze the effect of the fluoride treatment, we estimated the activation energy for carrier trapping (ΔE_T) by fitting the temperature-dependent integrated PL intensity, $I^{PL}(T)$, through the equation: $I^{PL}(T) = \frac{I_0^{PL}}{1+Ae^{-\Delta E_T/k_B T}}$, where, I_0^{PL} is the low temperature PL intensity and k_B is the Boltzmann constant. The data for the whole set of investigated PNCs are shown in Figure 3e; the obtained ΔE_T values are shown in Figure 3d. For the pristine PNCs, the trapping activation energy was found to be $\Delta E_T = 246$ meV, nearly matching the position of shallow states of bromine vacancies[39] that are typically located in energy between ~0.23 eV (ref.[40]) and ~0.16 eV (ref.[39]) above the CBM, thus corroborating the important role of halide vacancies on emission thermal quenching[34,41]. Upon increasing the DDAF amounts, ΔE_T increased, reaching $\Delta E_T = 644$ meV for F/Br=8.1% indicating that surface bromine vacancies are effectively passivated. The trends of ΔE_{TRAP} and θ_{MAX} vs. the F/Br ratio correlate nearly perfectly with each other, confirming a substantial role of the fluoride treatment in the outstanding thermal resistance of the $CsPbBr_3$:F PNCs. A schematic depiction of the effects of DDAF on the photophysics of $CsPbBr_3$ PNCs is shown in the inset of Figure 3e. The fluorine treatment also improved the optical stability of $CsPbBr_3$ PNCs under continuous heating conditions. This is shown in Figure 3f where we report the PL intensity of pristine and $CsPbBr_3$:F(8.1) PNCs during three thermal cycles between T=293K and T=373K. Consistent with Figure 3a and 2b, the fluorine treated PNCs exhibited nearly constant PL intensity at any stage of the thermal ramp, except for a very minor darkening at 373K. Importantly, the initial room temperature PL intensity value was fully recovered after each cycle indicating no damage to the PNCs. Conversely, the pristine PNCs showed a marked reversible drop of their PL intensity due to thermally activated trapping, and a growing irreversible PL darkening in full agreement with the results by Diroll *et al*[34]. This suggests that continuous heating induced irreversible deterioration of the PNCs – notice that no PL quenching was observed under continuous illumination at room temperature (Supplementary Figure 6). Treating the PNCs with bromine precursors, DDABr, also helped in mitigating the thermal quenching of $CsPbBr_3$ PNCs, although less effectively than the fluoride treatment and comparable suppression of emission thermal quenching could be obtained using NH_4F as a fluorine source without the long chain DDA counter cation (Supplementary Figure 7), indicating that the DDA moiety plays a minor role in the stabilization process.

Structural studies. Structural characterizations were performed to disambiguate the effects of fluoride on the thermal quenching behavior of $CsPbBr_3$ PNCs. X-ray diffraction (XRD) patterns (Figure 4a) confirmed that both pristine and fluoride treated PNCs present the diffraction peaks corresponding to the cubic phase of $CsPbBr_3$.

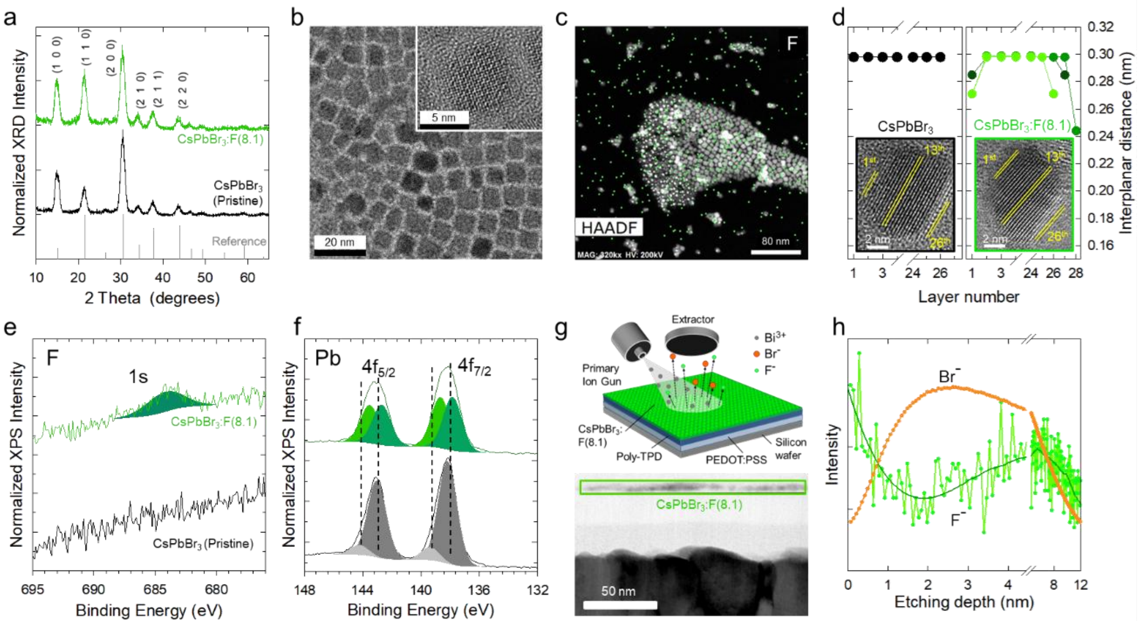

Figure 4. Structural characterization. (a) XRD patterns, (b) TEM (inset: corresponding HRTEM image) and (c) HAADF-STEM image of $CsPbBr_3$:F(8.1) PNCs superimposed to the respective EDS elemental mapping highlighting the presence of F. (d) Interplanar distance as a function of layer number in a single $CsPbBr_3$ pristine PNC (left plot) and in five different $CsPbBr_3$:F(8.1) PNC. The interplanar distance was precisely measured from the aberration-corrected STEM images reported in the inset. High-resolution XPS spectra of (e) F 1s and (f) Pb 4f elements. (g) Sketch of the experimental set-up used for the surface etching experiments. A cross sectional TEM image of tested sample is shown in the bottom panel. (h) Intensity signal corresponding to F^- (green circles) and Br^- (orange circles) measured with TOF-SIMS as a function of the etching depth for $CsPbBr_3$:F(8.1), showing the release of fluorine anions from the particles surfaces followed by bromine anions from the bulk.

Transmission electron microscopy (TEM) images (Figure 4b, Supplementary Figure 8) illustrate the average size of pristine (7.8 nm ± 0.9 nm) and $CsPbBr_3$:F(8.1) PNCs (6.9 nm ± 0.8 nm). The high-angle annular dark-field scanning transmission electron microscopy image (HAADF-STEM) and elemental mapping (Figure 4c, Supplementary Figure 9) highlight the presence of fluorine anions adsorbed onto the PNCs. Based on the higher electronegativity and smaller radius of fluorine with respect to bromine anions[42], leading to stronger chemical binding with Pb^{2+} (ref.[43-45]), it is reasonable to assume that fluorine anions occupy surface bromine vacancies and even exchange shallow bromine ions, likely resulting in fluorine-rich PNC surfaces. In-depth analysis of aberration-corrected STEM images supports this picture (Figure 4d and Supplementary Figures 10,11), revealing that the interplanar distance on the outer shell of $CsPbBr_3$:F(8.1) PNCs is significantly shorter than in the particle core, consistent with the smaller ionic radius of fluorine with respect to bromine. Therefore, we ascribe the lattice contraction to the presence of a fluorine-rich surface layer. This picture is corroborated by X-ray photoelectron spectroscopy (XPS) measurements (Figure 4e,f, Supplementary Figure 12). No significant changes were observed for 3d and Cs and Br core levels before and after introducing fluoride (Supplementary Figure 13). Most importantly, the spectra of F confirmed the presence of fluorine ions in treated PNCs and the Pb spectra revealed noticeable differences between pristine and treated PNCs. In both cases, the peaks of the 4f core level of Pb featured two components due to Pb cations in the inside and on the surfaces of the PNCs, respectively peaking at 144.6eV and 139.2eV and at 143.3eV and 138.1eV (ref.[46]). Before the treatment, the contribution of inner Pb cations dominated the XPS spectrum with nearly eight-fold intensity with respect to the surface lead. After treatment, due to the combination of fluorine and lead ions, the ratio between the two states of Pb changed dramatically, with the contribution of surface Pb matching that of inner Pb. The XPS changes of Pb further proved that fluorine ions occupied the surface Br sites, consistent with the DFT results. Further independent support to the formation of fluorine-rich surfaces in $CsPbBr_3$:F PNCs was provided by surface etching experiments using time-of-flight secondary-ion mass spectroscopy (TOF-SIMS) coupled to ionic sputtering. In full agreement with our structural and spectroscopic analysis, the signal intensity due to fluorine ions was maximum on the samples surfaces and dropped steeply in the first 2 nm (Figure 4h). Nearly perfect anticorrelation was found for the signal due to bromine ions, which were released mostly from the inner particle layers, thus corroborating the picture that the DDAF treatment modifies the particle surfaces leaving the $CsPbBr_3$ core unaltered.

Efficient, temperature stable LEDs. Finally, to experimentally validate our fluoride-treated PNCs as active materials in efficient, temperature resistant LEDs, we fabricated planar devices in the architecture depicted in Figure 5a. The corresponding flat-band energy diagram shown in Figure 5b was estimated from the ultraviolet photoelectron spectroscopy (Supplementary Figure 14). The EL spectrum is reported in Figure 5c together with the respective PL, showing a narrow (FWHM=20 nm) EL peak at 511 nm, redshifted with respect to the PL by ~2 nm, likely due to Stark effect.[47] No emission was observed from the organic interlayers under increasing bias voltage (3-8 V, Supplementary Figure 15), indicating that the injected carriers recombined at the PNCs.

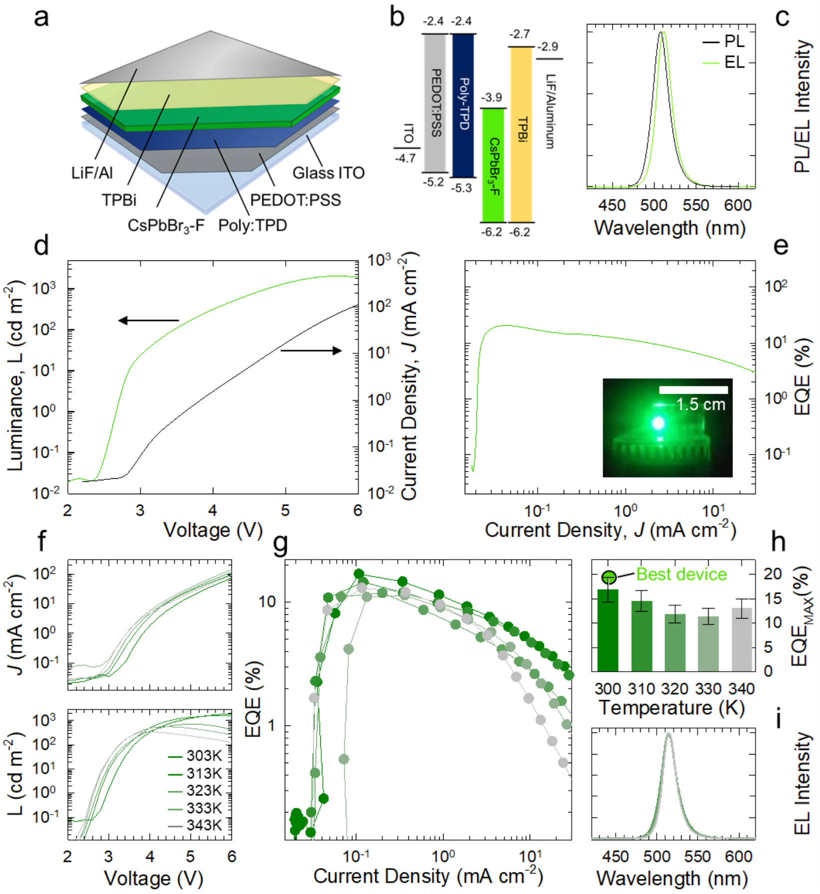

Figure 5 Thermally stable LEDs based on CsPbBr3:F nanocrystals. (a) Device structure and (b) flat band energy diagram of a multilayer LED. ITO: indium tin oxide; PEDOT:PSS: poly(3,4 ethylenedioxythiophene):polystyrene;.Poly-TPD: poly(N,N'-bis(4-butylphenyl)-N,N'-bis(phenyl) benzene); TPBi: (2,2′,2″-(1,3,5-benzinetriyl)-tris(1-phenyl-1-H-benzimidazole); LiF: Lithium fluoride; Al: Aluminium (c) EL spectrum of the LED and PL (405 nm excitation) spectrum of the $CsPbBr_3$:F(8.1) PNCs active layer. (d) Current density – Voltage – Luminance (*J*-V-L) response of the best device embedding $CsPbBr_3$:F(8.1) PNCs. (e) EQE vs. current density showing maximum efficiency of 19.3%. Inset: Photograph of a working LED (device area 4mm^2). (f) *J*-V (top panel) and L-V (bottom panel) curves of a representative LED with $CsPbBr_3$:F(8.1) PNCs active layer at increasing working temperature from 303K to 343 K. (g) EQE-Current density curves, (h) maximum EQE and (i) normalized EL spectrum as a function of temperature for the same device. The color scheme indicated in panel ‘f’ applies to panels f-i.

Figure 5d,e report the current density–voltage–luminance (*J*-V-L) response and the corresponding EQE vs. current density curve of the best LED without encapsulation at room temperature. The device turned on at V_{ON}= 2.7 V (defined as the voltage at which the luminance was 1cd/m^2) and exhibited EQE = 19.3%, and maximum luminance of 2030 cd/m^2. The corresponding internal QE calculated according to ref.[38] is 89%. The average EQE measured over 20 devices was 16.1% with standard deviation of 1.8%, indicating very good reproducibility of the device performance (Supplementary Table 3). By comparison, the average EQE of the LEDs with pristine PNCs was 0.13± 0.06% due to the presence of surface defects in the PNCs (*J*-V-L response and EQE of pristine $CsPbBr_3$ NCs LED are reported in Supplementary Figure 16), in agreement with previous reports[18]. The half-lifetime (T_{50}, defined as the time after which the luminance decreases of a factor of two) of unencapsulated devices operated at initial luminance of 1000 cd m^{-2} increased from T_{50}= 12 s for the pristine case, to T_{50}=50 s (at comparable L_0) for an LED embedding $CsPbBr_3$:F(8.1) PNCs (Supplementary Figure 17). By using the expression of L^nT_{50}=constant, and assuming an acceleration factor of n = 1.5 (ref.[21]), we estimate that the LED embedding fluorine-treated PNCs to exhibit T_{50}=25 minutes at 100 cd m^{-2}, which is comparable to the performance of stable literature PNC-LEDs tested in comparable conditions[12,13,17,48-50].

Finally, in order to assess the effect of the increased thermal resistance of fluoride treated PNCs on operating LEDs, we performed temperature stress measurements on an LED exhibiting maximum room temperature EQE of 16.9% and maximum luminance of 1946 cd/m^2 that better represented our device set. The *J*-V-L characteristics and the EQE curve of such an LED without encapsulation at increasing operating temperature from T=303 K to T=343 K (ambient condition, humidity 50% – 60%) are shown in Figure 5f and 5g respectively. In these experiments, the high-temperature limit of 343 K was imposed by the degradation of the Al cathode during the heating process as shown in Supplementary Figure 18. Upon increasing the temperature, V_{ON} decreased progressively from 3.0 V to 2.6 V, likely due to thermal-assisted carrier injection (Supplementary Table 4). Most importantly, the EQE decreased only to 13.0% when operated at T=343 K, which nearly matches the room temperature value within the experimental standard deviation (Figure 5h). This corresponds to a 23% drop, which is a substantial improvement with respect to LEDs embedding conventional $CsPbBr_3$ PNCs that have shown up to 90% efficiency drop in the same temperature range[36]. Based on the fact that the PL efficiency of the $CsPbBr_3$:F(8.1) PNCs is essentially constant at such a temperature, we speculate that the observed decreased of the EQE could be also due to thermal effects on the organic interlayers. Importantly, and in full agreement with the PL data in Figure 2a, the EL spectrum of our device is perfectly preserved at all investigated temperatures (Figure 5i), indicating perfect thermal resistance of the emission color purity. Finally, consistent with the partial mitigation of emission thermal quenching by Br-treatment, LEDs embedding $CsPbBr_3$ PNCs post-treated with DDABr also featured high EQE_{max} = 15.2% at 303 K (Supplementary Figure 19), but their efficiency dropped to ~3% at 343 K, in line with the PL vs. temperature trend shown in Supplementary Figure 7.

In summary, we have demonstrated a new fluoride post-synthesis treatment for that suppresses emission thermal quenching and improves the structural thermal stability of cesium lead halide PNCs, enabling temperature independent light emission up to 373 K. Using fluorine treated $CdPbBr_3$ PNC we obtained a LEDs with EQE as high as 19.3% at 303 K and temperature stress experiments showed a small, 23%, efficiency drop when operated at high temperatures. The fluoride treatment was demonstrated to be effective also for other lead halide perovskites covering the whole visible spectrum. Therefore, our results hold promise for the realization of high-efficiency and temperature-stable LEDs produced via solution-based process.

METHODS

Chemicals. Cesium carbonate (Cs_2CO_3, 98%), lead bromide ($PbBr_2$, 98%), sodium fluoride (NaF, 99%), didodecyl dimethylammonium bromide (DDABr, 98%), 1-octadecene (ODE, 90%), oleylamine (OAm, 90%), toluene (98%), methyl acetate (MeOAc, 98%) were purchased from Aladdin. Oleic acid (OA, 90%) was purchased from Sigma-Aldrich. All the chemical reagents were used directly without further purification.

Preparation of Cs-oleate precursor. 3.2582 g Cs_2CO_3 (10 mmol), 20 mL OA and 20 mL ODE were mixed in a three-neck flask and degassed at 120°C for 1 h under vacuum. Then the mixture was heated to 150°C under Ar until the solution transformed into clear and cooled down to room temperature for storing.

Preparation of DDAF precursor. 1.1566 g DDABr (2.5 mmol) and 105 mg NaF (2.5 mmol) were dissolved in 25 mL toluene and 25 mL ultra-pure water, respectively. Then these solutions were mixed under sonication for 30 min in order to exchange fluorine anions with bromine anions completely. Subsequently, the milky mixture was centrifuged and then the toluene solution was obtained as DDAF precursor (0.015mmol/mL).

Synthesis of $CsPbBr_3$ NCs. 0.734 g $PbBr_2$ (2 mmol), 20 mL ODE, 5 mL OA and 5 mL OAm were put into a three-neck flask and degassed at 120°C for 1 h under vacuum. Then the flask was filled with Ar and heated up to 180°C until $PbBr_2$ was dissolved completely. Subsequently, 1 mL pre-heated Cs-oleate precursor was swiftly injected into the flask to react for 10 seconds and then immerged into ice-water bath dramatically. The products were centrifuged with MeOAc and re-dispersed with toluene and the supernatant was obtained as $CsPbBr_3$ NCs stock solution.

Synthesis of $CsPbBr_3$·F or $CsPbBr_3$·DDABr NCs. In this procedure, certain amount of DDAF (or DDABr) solution was added into 1 mL $CsPbBr_3$/toluene stock solution to stir for 30 minutes at room temperature and then the mixture was centrifuged with MeOAc. The sediment was re-dispersed with toluene for centrifugation again and then the supernatant was collected as $CsPbBr_3$:F or $CsPbBr_3$:DDABr NCs solution.

Thermal quenching experiments. For temperature-dependent measurements, the pristine, fluoride post-treated, and bromine post-treated $CsPbBr_3$ NCs were diluted with toluene and then the solutions were heated gradually in an oil-bath. The *in-situ* PL spectra were recorded at certain temperature in the range of 293-373 K. We restricted our data analysis to 370K as the sudden drop of the PL intensity at 373 K is not due PL quenching but to enhanced mobility of toluene solvent when the temperature approaches its boiling point at 383.6 K, which introduced instability in the PL measurement.

Structural characterization. X-ray powder diffraction (XRD) patterns were recorded on a Bruker D8 ADVANCE diffractometer using Cu Kα radiation (40 kV, 30 mA, 2°/min from 10 to 80°, $\lambda = 1.5406$ Å). Samples of all perovskite NCs were prepared for high-resolution transmission electron microscope (HRTEM, FEI Talos F200X, operating at 200 kV) and aberration-corrected STEM (JEOL ARM-200F, operating at 200 kV). The surface composition and chemical state of samples were detected through X-ray photo-electron spectroscopy (XPS) using Kratos Axis Ultra DLD. Room temperature UV−vis absorption spectroscopy and PL spectra were recorded on a Cary-60 UV−vis spectrophotometer and F-380 fluorescence spectrometer (Tianjin Gangdong Sci. & Tech. Development Co., Ltd., China), respectively. Temperature-dependent fluorescence lifetimes were performed on a time-resolved fluorescence spectrofluorometer (QM/TM/IM, PTI, USA). In the surface etching experiments, a nearly single particle layer (~10 nm) of $CsPbBr_3$:F(8.1) was deposited onto a low-roughness Poly:TPD film and exposed to Bi^{3+} cations. The depth of the etching process was calibrated through Atomic Force Microscopy. For the time-of-flight secondary-ion mass spectrometry (TOF-SIMS) studies, TOF-SIMS 5-100 was used at analysis chamber pressure below 1.1×10^{-9} mbar. Depth analysis with delay extraction mode with pulsed 30 keV Bi^{3+} (0.05 pA pulsed current) ion beam was applied. Typical analysis area was 10×10 μm^2.

Device fabrication. The devices were assembled with the following structure: anode consisted in an indium tin oxide (ITO) coated glass substrate with PEDOT:PSS (thickness 35 nm) / Poly-TPD (thickness: 30 nm) hole injection/transport layers. On the cathode side, a 25 nm thick film of PNCs was overcoated with 40 nm of a TPBi electron transport layer separated from the Al cathode (100 nm) by 1 nm of LiF.

PEDOT:PSS solutions (Baytron P VPAl 4083, filtered through a 0.45 μm filter) were spin-coated onto the ITO-coated glass substrates at 4000 rpm for 20 seconds and baked at 145°C for 15 minutes. The poly-TPD chlorobenzene solution (8 mg mL^{-1}) was spin-coated at 4000 rpm for 20 seconds and annealed at 110°C for 20 minutes to form hole transporting layer before $CsPbBr_3$ NCs were deposited at 2000 rpm for 20 seconds. Then TPBi and LiF/Al electrodes were deposited using a thermal evaporation system through a shadow mask under a high vacuum.

Device efficiency characterization. A Keithley 2602 source meter (sweep rate 0.2V/s) was used to measure the current−voltage-luminance characteristics of the devices. The light output was measured by a calibrated silicon photodetector positioned at a fixed distance and directed toward the ITO glass side of the device. The LED brightness was determined from the fraction of light that reaches the photodetector. The EL spectra were recorded with a Spex 270 M spectrometer coupled to a charged couple device. LEDs were tested in nitrogen atmosphere without additional environmental protection. The devices were stored under ambient conditions between experiments. Stress tests were performed with the same equipment on unencapsulated LEDs in ambient conditions.

Data availability statement. The data that support the findings of this study are available from the corresponding author upon reasonable request

REFERENCES

1 Shamsi, J., Urban, A. S., Imran, M., De Trizio, L. & Manna, L. Metal halide perovskite nanocrystals: synthesis, post-synthesis modifications, and their optical properties. *Chem. Rev.* **119**, 3296-3348 (2019).

2 Akkerman, Q. A. *et al.* Strongly emissive perovskite nanocrystal inks for high-voltage solar cells. *Nature Energy* **2**, 16194 (2016).

3 Xing, G. *et al.* Low-temperature solution-processed wavelength-tunable perovskites for lasing. *Nat. Mater.* **13**, 476 (2014).

4 Meinardi, F. *et al.* Doped Halide Perovskite Nanocrystals for Reabsorption-Free Luminescent Solar Concentrators. *ACS Energy Lett.* **2**, 2368-2377 (2017).

5 Gandini, M. *et al.* Efficient, fast and reabsorption-free perovskite nanocrystal-based sensitized plastic scintillators. *Nat. Nanotech.* **15**, 462-468 (2020).

6 Song, J. *et al.* Quantum Dot Light-Emitting Diodes Based on Inorganic Perovskite Cesium Lead Halides ($CsPbX_3$). *Adv. Mater.* **27**, 7162-7167 (2015).

7 Pan, J. *et al.* Highly Efficient Perovskite-Quantum-Dot Light-Emitting Diodes by Surface Engineering. *Adv. Mater.* **28**, 8718-8725 (2016).

8 Chiba, T. *et al.* High-Efficiency Perovskite Quantum-Dot Light-Emitting Devices by Effective Washing Process and Interfacial Energy Level Alignment. *ACS Appl. Mater. Interfaces* **9**, 18054-18060 (2017).

9 Li, J. *et al.* 50-Fold EQE Improvement up to 6.27% of Solution-Processed All-Inorganic Perovskite $CsPbBr_3$ QLEDs via Surface Ligand Density Control. *Adv. Mater.* **29**, 1603885 (2017).

10 Song, J. *et al.* Room-Temperature Triple-Ligand Surface Engineering Synergistically Boosts Ink Stability, Recombination Dynamics, and Charge Injection toward EQE-11.6% Perovskite QLEDs. *Adv. Mater.* **30**, 1800764 (2018).

11 Song, J. *et al.* Organic–Inorganic Hybrid Passivation Enables Perovskite QLEDs with an EQE of 16.48%. *Adv. Mater.* **30**, 1805409 (2018).

12 Yan, F. *et al.* Highly Efficient Visible Colloidal Lead-Halide Perovskite Nanocrystal Light-Emitting Diodes. *Nano Lett.* **18**, 3157-3164 (2018).

13 Chen, H. *et al.* Sodium Ion Modifying In Situ Fabricated $CsPbBr_3$ Nanoparticles for Efficient Perovskite Light Emitting Diodes. *Advanced Optical Materials* **7**, 1900747 (2019).

14 Dong, Y. *et al.* Bipolar-shell resurfacing for blue LEDs based on strongly confined perovskite quantum dots. *Nat. Nanotech.* **15**, 668-674 (2020).

15 Xing, J. *et al.* High-Efficiency Light-Emitting Diodes of Organometal Halide Perovskite Amorphous Nanoparticles. *ACS Nano* **10**, 6623-6630 (2016).

16 Han, D. *et al.* Efficient Light-Emitting Diodes Based on in Situ Fabricated $FAPbBr_3$ Nanocrystals: The Enhancing Role of the Ligand-Assisted Reprecipitation Process. *ACS Nano* **12**, 8808-8816 (2018).

17 Chen, H. *et al.* High-Efficiency Formamidinium Lead Bromide Perovskite Nanocrystal-Based Light-Emitting Diodes Fabricated via a Surface Defect Self-Passivation Strategy. *Advanced Optical Materials* **8**, 1901390 (2020).

18 Chiba, T. *et al.* Anion-exchange red perovskite quantum dots with ammonium iodine salts for highly efficient light-emitting devices. *Nat. Photon.* **12**, 681-687 (2018).

19 Lee, S. *et al.* Growth of Nanosized Single Crystals for Efficient Perovskite Light-Emitting Diodes. *ACS Nano* **12**, 3417-3423 (2018).

20 Ban, M. *et al.* Solution-processed perovskite light emitting diodes with efficiency exceeding 15% through additive-controlled nanostructure tailoring. *Nat. Commun.* **9**, 3892 (2018).

21 Lin, K. *et al.* Perovskite light-emitting diodes with external quantum efficiency exceeding 20 per cent. *Nature* **562**, 245-248 (2018).

22 Cao, Y. *et al.* Perovskite light-emitting diodes based on spontaneously formed submicrometre-scale structures. *Nature* **562**, 249-253 (2018).

23 Zhao, B. *et al.* High-efficiency perovskite–polymer bulk heterostructure light-emitting diodes. *Nat. Photon.* **12**, 783-789 (2018).

24 Xu, W. *et al.* Rational molecular passivation for high-performance perovskite light-emitting diodes. *Nat. Photon.* **13**, 418-424 (2019).

25 Lee, H., Ko, D. & Lee, C. Direct Evidence of Ion-Migration-Induced Degradation of Ultrabright Perovskite Light-Emitting Diodes. *ACS Appl. Mater. Interfaces* **11**, 11667-11673 (2019).

26 Palazon, F. *et al.* Evolution of $CsPbBr_3$ nanocrystals upon post-synthesis annealing under an inert atmosphere. *J. Mater. Chem. C* **4**, 9179-9182 (2016).

27 Conings, B. *et al.* Intrinsic thermal instability of methylammonium lead trihalide perovskite. *Adv. Energ. Mater.* **5**, 1500477 (2015).

28 Bachmann, V., Ronda, C. & Meijerink, A. Temperature quenching of yellow Ce^{3+} luminescence in YAG: Ce. *Chem. Mat.* **21**, 2077-2084 (2009).

29 Ahn, B.-L., Jang, C.-Y., Leigh, S.-B., Yoo, S. & Jeong, H. Effect of LED lighting on the cooling and heating loads in office buildings. *Applied Energy* **113**, 1484-1489 (2014).

30 Wei, Y., Cheng, Z. & Lin, J. An overview on enhancing the stability of lead halide perovskite quantum dots and their applications in phosphor-converted LEDs. *Chem. Soc. Rev.* **48**, 310-350 (2019).

31 Zhang, F. *et al.* Brightly luminescent and color-tunable colloidal $CH_3NH_3PbX_3$ (X= Br, I, Cl) quantum dots: potential alternatives for display technology. *ACS Nano* **9**, 4533-4542 (2015).

32 Li, X. *et al.* $CsPbX_3$ quantum dots for lighting and displays: room-temperature synthesis, photoluminescence superiorities, underlying origins and white light-emitting diodes. *Adv. Funct. Mater.* **26**, 2435-2445 (2016).

33 Wei, S. *et al.* Room-temperature and gram-scale synthesis of $CsPbX_3$ (X= Cl, Br, I) perovskite nanocrystals with 50–85% photoluminescence quantum yields. *Chem. Commun.* **52**, 7265-7268 (2016).

34 Diroll, B. T., Nedelcu, G., Kovalenko, M. V. & Schaller, R. D. High-Temperature Photoluminescence of $CsPbX_3$ (X= Cl, Br, I) Nanocrystals. *Adv. Funct. Mater.* **27**, 1606750 (2017).

35 Zhang, Q. *et al.* Bifunctional Passivation Strategy to Achieve Stable $CsPbBr_3$ Nanocrystals with Drastically Reduced Thermal-Quenching. *J. Phys. Chem. Lett.* **11**, 993-999 (2020).

36 Shi, Z. *et al.* Strategy of solution-processed all-inorganic heterostructure for humidity/temperature-stable perovskite quantum dot light-emitting diodes. *ACS Nano* **12**, 1462-1472 (2018).

37 Kohn, W. & Sham, L. J. Self-consistent equations including exchange and correlation effects. *Phys. Rev.* **140**, A1133 (1965).

38 Wang, N. *et al.* Perovskite light-emitting diodes based on solution-processed self-organized multiple quantum wells. *Nat. Photon.* **10**, 699-704 (2016).

39 Shi, H. & Du, M.-H. Shallow halogen vacancies in halide optoelectronic materials. *Phys. Rev. B* **90**, 174103 (2014).

40 Sebastian, M. *et al.* Excitonic emissions and above-band-gap luminescence in the single-crystal perovskite semiconductors $CsPbBr_3$ and $CsPbCl_3$. *Phys. Rev. B* **92**, 235210 (2015).

41 Righetto, M. *et al.* Hot carriers perspective on the nature of traps in perovskites. *Nat. Commun.* **11**, 2712 (2020).

42 Li, N. *et al.* Cation and anion immobilization through chemical bonding enhancement with fluorides for stable halide perovskite solar cells. *Nature energy* **4**, 408 (2019).

43 Castelli, I. E., García-Lastra, J. M., Thygesen, K. S. & Jacobsen, K. W. Bandgap calculations and trends of organometal halide perovskites. *APL Materials* **2**, 081514 (2014).

44 Li, C. *et al.* Halide-Substituted Electronic Properties of Organometal Halide Perovskite Films: Direct and

Inverse Photoemission Studies. *ACS Appl. Mater. Interfaces* **8**, 11526-11531 (2016).

45 Chen, Q. *et al.* Under the spotlight: The organic–inorganic hybrid halide perovskite for optoelectronic applications. *Nano Today* **10**, 355-396 (2015).

46 Woo, J. Y. *et al.* Highly stable cesium lead halide perovskite nanocrystals through in situ lead halide inorganic passivation. *Chem. Mat.* **29**, 7088-7092 (2017).

47 Empedocles, S. A. & Bawendi, M. G. Quantum-confined stark effect in single CdSe nanocrystallite quantum dots. *Science* **278**, 2114-2117 (1997).

48 Di Stasio, F. *et al.* High-Efficiency Light-Emitting Diodes Based on Formamidinium Lead Bromide Nanocrystals and Solution Processed Transport Layers. *Chem. Mat.* **30**, 6231-6235 (2018).

49 Tan, Y. *et al.* Highly Luminescent and Stable Perovskite Nanocrystals with Octylphosphonic Acid as a Ligand for Efficient Light-Emitting Diodes. *ACS Appl. Mater. Interfaces* **10**, 3784-3792 (2018).

50 Yang, F. *et al.* Efficient and Spectrally Stable Blue Perovskite Light-Emitting Diodes Based on Potassium Passivated Nanocrystals. *Adv. Funct. Mater.* **30**, 1908760 (2020).

Acknowledgements

This work was supported by the National Key Research and Development Program (No. 2017YFE0127100), Guangdong Province's 2018-2019 Key R&D Program (2019B010924001), National Natural Science Foundation of China (NSFC 21773155), Shanghai Sailing Program (19YF1422200), Shanghai Jiao Tong University Scientific and Technological Innovation Funds, and Engineering Research Center for Nanophotonics & Advanced Instrument, the Ministry of Education, East China Normal University (no. 202001). Financial support from the Italian Ministry of University and Research (MIUR) through grant “Dipartimenti di Eccellenza- 2017 "Materials For Energy”. We thank the instrumental analysis center of Shanghai Jiao Tong University and the workers (Jiaxin Ding, Xue Ding, Nannan Zhang, Xinqiu Guo and Yao Han) for the help of XPS, TOF-SIMS and TEM analysis. We also acknowledge Haili Song from school of chemistry of Sun Yat-sen University for the help of aberration-corrected STEM measurements.

AUTHOR INFORMATION

Statement of author contribution

L.L conceived this study. M.L. synthesized and characterized the nanocrystals and performed the thermal quenching experiments. Q.W fabricated and tested the LEDs. H.W. and X.S performed the DFT calculations. F.C. performed the optical characterization under the supervision of S.B. M.L. and W.Z. with the assistance of Q.G.Z.; L.K., Q.Z., and C.Z. performed the structural characterization. L.L and S.B. analyzed the data. S.B. wrote the paper in consultation with all authors.

Corresponding Authors

*E-mail: liangli117@sjtu.edu.cn; *E-mail: sergio.brovelli@unimib.it

Ethics declarations

The authors declare no competing financial interest.